A Novel GNSS Integrity Augmentation System for Civil and Military Aircraft

Roberto Sabatini, Terry Moore, Chris Hill

Abstract—This paper presents a novel Global Navigation Satellite System (GNSS) Avionics Based Integrity Augmentation (ABIA) system architecture suitable for civil and military air platforms, including Unmanned Aircraft Systems (UAS). Taking the move from previous research on high-accuracy Differential GNSS (DGNSS) systems design, integration and experimental flight test activities conducted at the Italian Air Force Flight Test Centre (CSV-RSV), our research focused on the development of a novel approach to the problem of GNSS ABIA for mission- and safety-critical air vehicle applications and for multi-sensor avionics architectures based on GNSS. Detailed mathematical models were developed to describe the main causes of GNSS signal outages and degradation in flight, namely: antenna obscuration, multipath, fading due to adverse geometry and Doppler shift. Adopting these models in association with suitable integrity thresholds and guidance algorithms, the ABIA system is able to generate integrity cautions (predictive flags) and warnings (reactive flags), as well as providing steering information to the pilot and electronic commands to the aircraft/UAS flight control systems. These features allow real-time avoidance of safety-critical flight conditions and fast recovery of the required navigation performance in case of GNSS data losses. In other words, this novel ABIA system addresses all three cornerstones of GNSS integrity augmentation in mission- and safety-critical applications: prediction (caution flags), reaction (warning flags) and correction (alternate flight path computation).

Keywords—Global Navigation Satellite Systems (GNSS), Integrity Augmentation, Unmanned Aircraft Systems, Aircraft Based Augmentation, Avionics Based Integrity Augmentation, Safety-Critical Applications.

I. INTRODUCTION

THE aerospace community has very stringent navigation integrity requirements, which apply to a variety of mission- and safety-critical operational tasks. Current and likely future air platforms are equipped with a variety of navigation sensors and systems. These sensors/systems can be used in a suitable integrated architecture to enhance integrity levels, therefore matching the requirements of mission/safety-critical navigation and lading tasks both in military and civil aircraft. A novel and properly conceived technique providing Avionics Based Integrity Augmentation (ABIA) could have a significant impact on the aerospace community, with the potential of being selected as a suitable technology for the future global Air Traffic Management (ATM) system, possibly within the framework of NextGen/SESAR developments (i.e., in association with other CNS/ATM technologies like ABS-B, RNAV and Aeronautical Data Links). In recent years, various strategies have been developed for increasing the levels of integrity of GNSS based navigation/landing systems. In addition to Space Based Augmentation Systems (SBAS) and Ground Based Augmentation Systems (GBAS), GNSS augmentation may also take the form of additional information being provided by other avionics systems. In most cases, the additional avionics systems operate via separate principles than the GNSS and, therefore, are not subject to the same sources of error or interference. A system such as this is referred to as an Avionics-Based or Aircraft-Based Augmentation System (ABAS). The additional sensors may include Inertial Navigation Systems (INS), VOR/DME, Radar, Electro-Optical Sensors, Automated Celestial Navigation, Dead Reckoning, etc. Unlike SBAS and GBAS technology, published research on ABAS is limited and mainly concentrates on additional information being blended into the position calculation to increase accuracy and/or continuity of the integrated navigation solutions. Additionally, no significant attempts have been made of developing ABAS architectures capable of generating integrity signals suitable for safety-critical GNSS applications (e.g., aircraft precision approach and landing) and no commercial ABAS products are available at present. Although current and likely future SBAS/GBAS augmentation systems can provide significant improvement of GNSS navigation performance, a properly designed and flight certified ABAS system could play a key role in GNSS Integrity Augmentation for safety-critical applications such as aircraft precision approach and automatic landing. Furthermore, using suitable data link and data processing technologies on the ground, a certified ABAS capability could be a core element of a future GNSS Space-Ground-Avionics Augmentation Network (SGAAN).

R. Sabatini is Associate Professor in the School of Aerospace, Mechanical and manufacturing Engineering, RMIT University, Melbourne, VIC 3000, Australia. Formerly, he was Senior Officer and Experimental Flight Test Engineer in the Italian Air Force, Pratica di Mare AFB, 00040 Pomezia (RM), Italy (phone: +61 3 9925 8015; e-mail: roberto.sabatini@rmit.edu.au).

T. Moore is Full Professor and the Director of the Nottingham Geospatial Institute, University of Nottingham, Nottingham, NG7 2TU, United Kingdom (e-mail: terry.moore@nottingham.ac.uk).

C. Hill is Principal Research Officer at the Nottingham Geospatial Institute, University of Nottingham, Nottingham, NG7 2TU, United Kingdom (e-mail: chris.hill@nottingham.ac.uk).

II. DGNSS RESEARCH ACTIVITIES

In recent years, the Italian Air Force Flight Test Centre was responsible for several flight test campaigns in which Differential GNSS (DGNSS) Time and Space Position Information (TSPI) systems were employed. These activities included [1]:

1) MB-339CD DGPS In-flight Evaluation of Two Off-the-shelf Receivers (Data Continuity);

2) TORNADO-IDS DGPS Data Continuity and Accuracy Evaluation;
3) EF-2000 (TYPHOON) DGPS Data Continuity, Accuracy and Integrity Evaluation.

During the MB-339CD avionics flight trials, an in-flight evaluation of DGPS was carried out. The aim of this assessment was to compare the performance of various ASHTECH and TRIMBLE GPS receivers in a dynamic environment, in order to select the system with the best performance for employment in future activities. Particularly, the assessment focused on the data continuity provided by the two GPS receivers during execution of low, medium, and high dynamics maneuvers and re-acquisition times after GPS data losses. Analyzing several data from the MB-339CD DGPS test campaign and other flight test activities performed with DGPS instrumented aircraft (i.e., F104 ASA-M, AM-X, EF-2000, MB-339A, TORNADO-IDS, etc.), it was clear that the main disadvantage of the GPS is its vulnerability to signal losses caused by satellites masking and low SNR. Therefore, during some TORNADO-IDS flight trials these problems were thoroughly investigated, to test the capability of the on-board GPS receiver to reacquire satellite signals and to provide TSPI even with degraded satellite constellations. In order to assist in the investigation a simulation tool was used to evaluate the global masking effect due to antenna and aircraft body masking. A preliminary assessment was also carried out of Doppler effects influence on data quality. Moreover, appropriate procedures were defined for the optimal use of DGPS (continuous positioning data gathering with reduced satellite signal losses) in flight test activities with high performance aircraft. Finally, an assessment of DGPS data accuracy was carried out, by comparing the positioning data provided by DGPS with other known references (laser tracking, optical systems, etc.). The detailed results of these experimental case studies are reported in [1].

III. INTEGRITY AUGMENTATION

GNSS augmentation benefits in the aviation domain can be summarized as follows:
1) Increased Runway Access;
2) More direct en route flight paths;
3) New precision approach services;
4) Reduced and simplified avionics equipment;
5) Potential elimination of some ground-based navigation aids (VOR, ILS, etc.) with cost saving to Air Navigation Service Providers (ANSPs).

Integrity relates to the level of trust that can be placed in the information provided by the navigation system [2]. It includes the ability of the navigation system to provide timely and valid warnings to users when the system must not be used for the intended operation or phase of flight. Specifically, a navigation system is required to deliver a warning (an alert) of any malfunction (as a result of a set alert limit being exceeded) to users within a given period of time (time-to-alert). Integrity risk also referred to as the probability of misleading information, is defined as the probability that the navigation positioning error exceeds the alert limit and that the event is

not detected. Loss of integrity can happen in one of two ways. Either an unsafe condition is not detected or it is detected, but the alert is not received by the user within the time-to-alert. The alert limit defines the largest position error, which results in a safe operation. This is specified such that the error can degrade to a level larger than the 95th percentile accuracy requirement but still within a safe limit. Time-to-alert (TTA) is defined as the maximum time allowed from the moment a fault resulting in an unsafe condition is detected to the moment that the user is made aware of it.

A. Avionics Based Integrity Augmentation

The ABIA concept is very different from RAIM (Receiver Autonomous Integrity Monitoring), in which the aircraft characteristics (flight dynamics, body shape, antenna location, EMC/EMI) are not considered. Based on the results of the DGPS TSPI research activities, we designed an ABIA system specifically targeting GNSS integrity augmentation in TSPI applications (Fig. 1). In this ABIA system, the aircraft sensors provide information on the aircraft relevant flight parameters (navigation data, engine settings, etc.) to an Integrity Flag Generator (IFG), which is also connected to the on-board GNSS. The IFG can be incorporated into one of the existing airborne computers or can be a dedicated processing unit. Using the available data on GNSS and the aircraft flight parameters, integrity signals are generated which can be displayed on one of the cockpit displays and/or sent to an Aural Warning Generator (AWG).
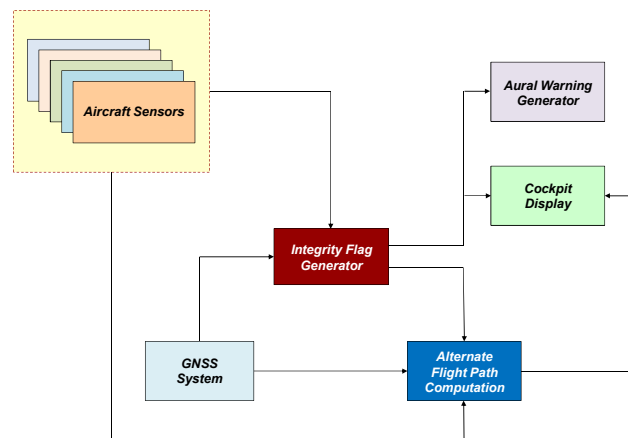

Fig. 1 ABIA system for flight test applications

The next logical step is to extend the results obtained from modeling, simulation and flight test to the design of a complete GNSS ABIA system suitable for manned and unmanned aircraft applications. Such a system, would be able to provide steering information to the pilot (as the ABIA system for flight test applications) and, possibly, electronic commands to the aircraft/UAS Flight Control System (FCS), allowing for real-time and continuous integrity monitoring, avoidance of safety/mission-critical flight conditions and fast recovery of the Required Navigation Performance (RNP) in

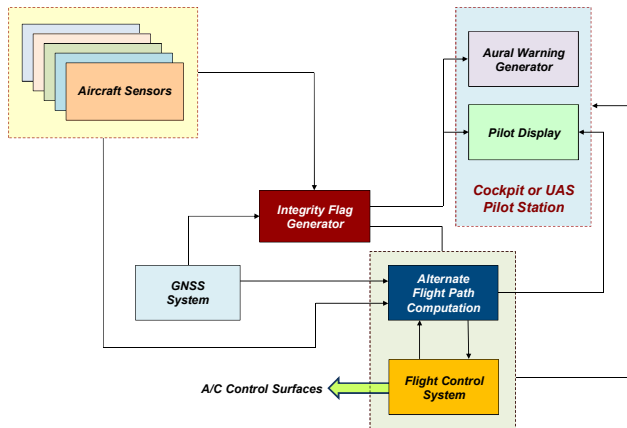case of GNSS data degradation or loss. The architecture of this advanced ABIA system is depicted in Fig. 2.

Fig. 2 ABIA evolution for manned and unmanned aircraft

B. ABIA Integrity Flags and TTA Definitions

The systems described above address both the predictive and reactive nature of GNSS integrity augmentation. To understand this concept, let us first of all introduce the definitions of alerts and TTA's applicable to the ABIA system:

1) <u>Caution Integrity Flag (CIF)</u>–This is a predictive annunciation that the GNSS data delivered to the avionics system is going to exceed the Required Navigation Performance (RNP) thresholds specified for the current and planned flight operational tasks (GNSS alert status).
2) <u>Warning Integrity Flag (WIF)</u>–This is a reactive annunciation that the GNSS data delivered to the avionics system has exceeded the Required Navigation Performance (RNP) thresholds specified for the current flight operational task (GNSS fault status).
3) <u>Time-to-Caution (TTC)</u>–This is the minimum time allowed for the caution flag to be provided to the user before the onset of a GNSS fault resulting in an unsafe condition.
4) <u>Time-to-Warning (TTW)</u>–This is the maximum time allowed from the moment a GNSS fault resulting in an unsafe condition is detected to the moment that the ABIA system provides a warning flag to the user.

IV. ABIA IFG MODULE DESIGN

The main causes of GNSS positioning data degradation or loss at aircraft level are:

1) Antenna obscuration;
2) Bad satellite geometry (PDOP);
3) Fading (low SNR);
4) Doppler shift;
5) Multipath effect (SNR, ranging and phase errors).

Understanding the physics of these phenomena and developing suitable mathematical models is essential in order to properly design the ABIA IFG module. Fig. 3 shows the architecture of the simulator used to validate the IFG design

for manned/unmanned platforms and to evaluate the TTA performance of the IFG (caution and warning flags) in various representative operational conditions.
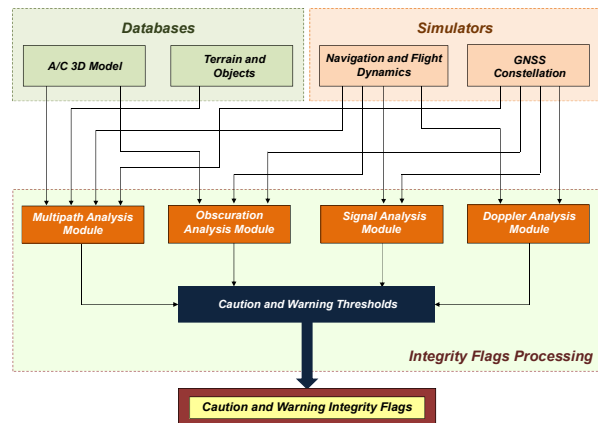

Fig. 3 IFG module simulation

A GNSS constellation simulator (GCS) was implemented to support GNSS satellite visibility, signal and geometry analysis. Using CATIA-P3, a detailed aircraft (A/C) 3-Dimensional Model (3DM) was developed and an Aircraft Dynamics Simulator (ADS) was implemented to generate the nominal flight path trajectory and attitude (Euler) angles. Terrain and Objects Data (TOD) is also required to run the MPS. Using a Digital Terrain Elevation Database (DTED), it is possible to obtain a detailed map of the terrain beneath the aircraft. Providing the aircraft trajectory inputs from the ADS module, terrain elevation data can be automatically extracted and fed to the TOM module where they are integrated with the database of man-made objects (e.g., buildings). The Doppler Simulator Module (DSM) calculates the Doppler shift by processing ADS and GCS inputs. The Multipath Analysis Module (MAM) process the 3DM, TEM, GCS and ADS inputs to determine multipath contributions from the aircraft (wings/fuselage) and from the terrain/objects close to the aircraft. The Obscuration Analysis Module (OAM) receives inputs from the 3DM, GCS and ADS, and computes the GNSS antenna (e) masking matrixes for all A/C maneuvers. The SNR Analysis Module (SAM) calculates the nominal link budget of the direct GNSS signals received by the aircraft in the presence of ionospheric and tropospheric propagation disturbances. The Integrity Flags Simulator (IFS) uses a set of predefined threshold parameters to trigger the generation of both caution and warning flags associated with antenna obscuration, Doppler shift, multipath, SNR, and satellite geometry degradations. The various modules implemented in the simulation and the techniques adopted to define the IFS integrity thresholds are described in the following paragraphs.

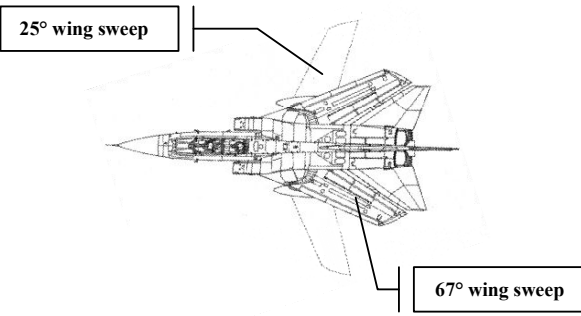### A. GNSS Constellation Simulator

The GNSS constellation simulator (GCS) was developed to calculate GNSS satellite position and velocity in the Earth-Centered Earth-Fixed (ECEF) reference frame and to obtain satellite visibility data from any point along the aircraft flight

trajectory. The initial version of the GCS was implemented in MATLAB to simulate GPS and GALILEO constellations. However, the GCS was developed as a flexible tool capable to incorporate other current and likely future GNSS constellations (GLONASS, COMPASS, etc.), including space-based regional and global augmentation systems. With reference to Fig. 7, the GCS output is used by the MAM, OAM and SAM modules, as well as by the IFS. The satellite position and velocity are calculated from the Kepler's laws of orbital motion using the YUMA or SEM almanac data [3], [4].

B. Aircraft 3-D Model

As an example, we consider the TORNADO aircraft. Various geometric parameters are required to draw a detailed CATIA (Computer Aided Three-dimensional Interactive Application) model of the aircraft. The main parameters are listed in Table I [5].

TABLE I
TORNADO DIMENSIONS

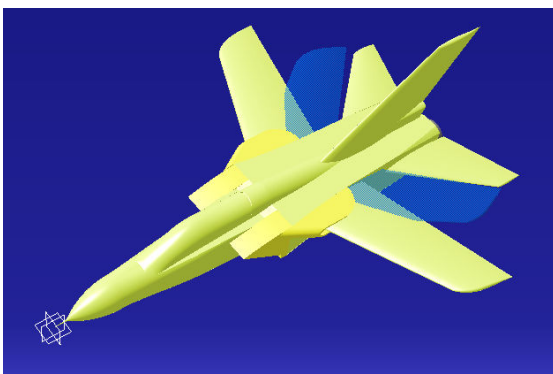| Length	16.72 m (54 ft10 in)
Wingspan	13.91 m at 25° wing sweep (45.6 ft)
	8.60 m at 67° wing sweep (28.2 ft)
Height	5.95 m (19.5 ft)
Wing area	26.6 m² (286 ft²)

The TORNADO 3-D CATIA model is shown in Fig. 4.

Fig. 4 TORNADO 3-D CATIA model

When calculating the antenna masking matrix and the corresponding satellite visibility, the antenna location must be included in the model. Military aircraft typically have an upper antenna at the top of the fuselage and a lower antenna at the base of the fuselage. In our case, the upper antenna is assumed to be located 1.5m behind the cockpit along the aircraft centerline projection and 5cm high on the aircraft skin surface [1]. The lower antenna is assumed to be right below the upper antenna on the opposite side of the fuselage (Fig. 5).
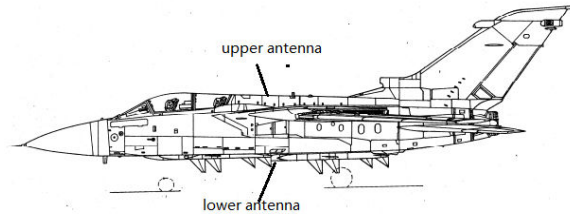

Fig. 5 TORNADO antennae locations

When calculating the satellite visibility, the line of sight (LOS) is measured in the antenna frame (i.e., origin at the antenna focal point). The transformation from body-frame to antenna frame is obtained from:

$$F_{antenna} = F_{body} + T_{body}^{antenna}(m) \qquad (1)$$

The transformation matrixes for the upper and lower antennae are:

$$T_{body}^{upper} = \begin{bmatrix} -0.88 \\ 0 \\ -0.74 \end{bmatrix}(m) \qquad (2)$$

$$T_{body}^{lower} = \begin{bmatrix} -0.88 \\ 0 \\ 2.13 \end{bmatrix}(m) \qquad (3)$$

C. Flight Dynamics Simulator

The Flight Dynamics Simulator (FDS) uses a 3 Degrees of Freedom (3-DOF) model with variable mass to calculate the trajectory of the aircraft (i.e., position, velocity and attitude angles) during the different flight phases. The assumption adopted in this model is:

1) The earth shape is approximated as an ellipsoid using WGS-84 parameters.
2) The atmosphere is considered at rest relatively to the earth and a standard ISA atmospheric model is adopted defining temperature, pressure and density as a function of altitude.
3) The aircraft is modeled as a rigid body with a vertical plane of symmetry.
4) The mass of the aircraft in flight varies (decreases) only due to fuel consumption.
5) Forces acting on the centre of gravity of the airplane are the thrust, aerodynamic forces and the weight.
6) The flight is supposed to be symmetric (no sideslip).

The 3-DOF scalar equations are the following:

$$m\frac{dV}{dt} = Tcos\alpha - D(V,h,L) - mgsin\gamma \qquad (4)$$

$$mV \frac{d\gamma}{dt} = (Tsin\alpha + L)cos\phi - mgcos\gamma \qquad (5)$$

$$mV \frac{d\psi}{dt} = (Tsin\alpha + L)\frac{sin\phi}{\cos\gamma} \qquad (6)$$

$$\frac{dm}{dt} = -c(V,h)T \qquad (7)$$

$$\frac{d\Phi}{dt} = \frac{Vcos\gamma cos\,\psi}{r_M + h} \qquad (8)$$

$$\frac{d\theta}{dt} = \frac{Vcos\gamma sin\,\psi}{\cos(\Phi)(r_T + h)} \qquad (9)$$

$$\frac{dh}{dt} = Vsin\gamma \qquad (10)$$

where:

m = Aircraft mass;
V = Aerodynamic speed;
T = Thrust magnitude;
α = Angle of attack;
h = Altitude;
L = Lift magnitude;
D = Drag, defined as a function of V, h and L;
g = Gravity acceleration;
γ = Flight path angle;
ϕ = Bank or roll angle;
ψ = Heading angle;
c = Specific fuel consumption (a function of V and h);
Φ = Geodetic latitude;
θ = Geodetic longitude;
r_M = Meridional radius of curvature;
r_T = Transverse radius of curvature.

This model presents seven state variables $(V, \psi, \gamma, m, \Phi, \theta, h)$ and three control variables (T, L, ϕ). Hence, for it to be solved, at least three flight constraints must be specified for each flight maneuver.

D. Satellite Masking Analysis

Due to the maneuvers of the aircraft, the wings, tail and fuselage will obscure some satellites during the flight. Fig. 6 shows the structure of the Satellite Masking Analysis (SMA) module. Taking into account the aircraft shape (CATIA 3-D model), the A/C flight dynamics (pitch, roll and yaw variations) and the information provided by the GCS, an global Antenna Masking Matrix (AMM) is generated for the different flight maneuvers possible. An example of the resulting Global Antenna Masking Matrix (AMM) obtained taking into account both bank (B) and pitch (P) angle variations is shown in Fig. 7. Besides the AMM, other factors influence the satellite visibility. In general, a satellite is geometrically visible to the GNSS receiver only if its elevation in the antenna frame is above the Earth horizon and the antenna elevation mask.
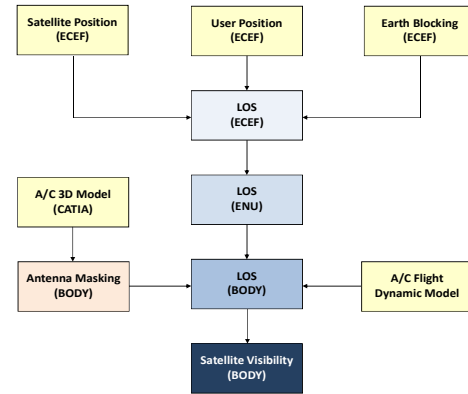

Fig. 6 GNSS satellite obscuration simulator

It should be noted that even high performance avionics GNSS antennas have a gain patterns that is typically below -3dB at about 5 degrees elevation [6] and, as a consequence, their performance become marginal below this limit.
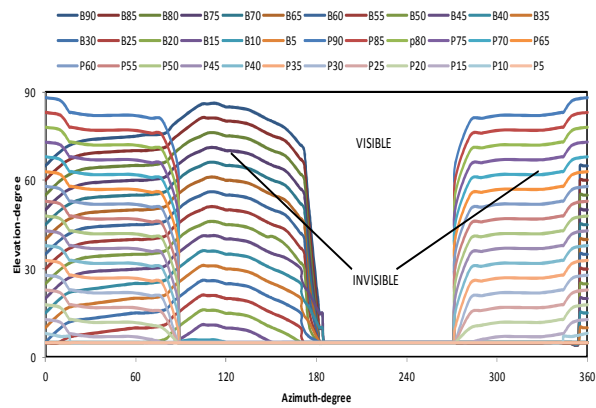
Fig. 7 Global Masking Envelope

In order to determine if a satellite is obscured, the LOS of the satellite with respect to the antenna phase centre has to be determined. To calculate the satellite azimuth and elevation with respect to the antenna the transformation matrix between ECEF (Earth Centered Earth Fixed) and the antenna frame must be applied. This transformation is obtained as follows:

$$T_E^a = T_b^a * T_N^b * T_E^N \qquad (11)$$

where T_b^a is the transformation matrix between the aircraft body frame and the antenna frame, T_N^b is the transformation matrix from ENU (East-North-Up) to body frame, and T_E^N is the ECEF to ENU transformation matrix. As an example, Fig. 8 shows the trajectory of a TORNADO aircraft during a turning descent maneuver lasting 300 seconds (spiral flight with a constant turn radius) and Fig. 9 shows the combined GPS/GALILEO satellite visibility during the same flight phase.

Fig. 8 TORNADO turning descent maneuver

The number of satellites in view varies from 7 to 16 during this flight maneuver.

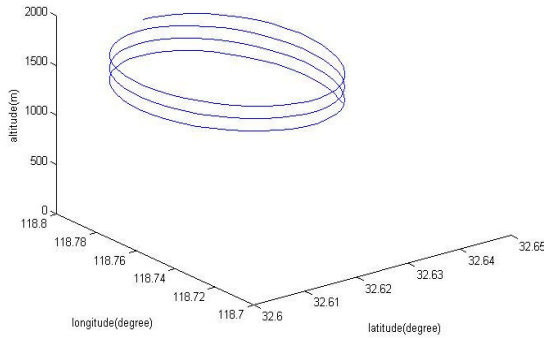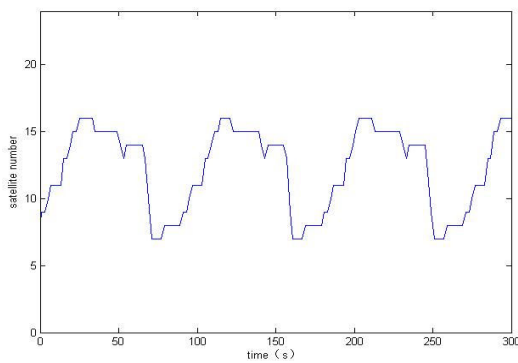Fig. 9 Satellite Visibility (TORNADO TDP)

E. Link Budget Analysis (Multipath Free)

The SNR at the receiver is affected by a number of factors. These factors include both transmitter and receiver characteristics, as well as propagation losses and interferences. In our simulation, the SNR Analysis Module (SAM) combines the various factors contributing to the GNSS signal fading. Multipath induced effects are considered separately. The SAM module takes inputs from the GCS and FDS modules, and computes SNR. In practice, the ratio of total carrier power to noise C/N_0 in dB-Hz is the most generic representation of received signal strength. This is given by:

$$\frac{C}{N_0} = P + G_T + G_R + SL - L_1 - L_2 - \sigma_m - N_F (dB) \qquad (12)$$

where:
P = Transmitted power
G_T = Satellite antenna gain
G_R = Receiver antenna gain
SL = Free Space Loss
L_1 = Atmospheric attenuation (dry-air)
L_2 = Rainfall attenuation
σ_m = Tropospheric fading
N_F = Receiver noise figure

Considering the bandwidth of the filter in the receiver (B_n), the GNSS link budget can be calculated from [6]:

$$SNR(dB) = \frac{S}{N} = \frac{C}{N_0} (dB - Hz) - B_n(dB) \qquad (13)$$

The link budget calculated from (13) only refers to the direct GNSS signal received from a satellite. Multipath effects, which are due to the geometric and reflective characteristics of the environment surrounding the GNSS antenna are not included in this calculation and are discussed separately. The L-band antenna onboard GPS satellites are designed to radiate the composite L-band signals to the users on and near the Earth. As shown in Fig. 10, the GPS satellite viewing angle from edge-to-edge of Earth is about 27.7 degrees [7]. The satellite antenna is designed to illuminate the Earth's surface with an almost uniform signal strength. The path loss of the signal is a function of the distance from the antenna phase centre to the surface of the Earth. The path loss is minimum when the satellite is directly overhead (satellite at 90 degrees elevation), and is maximum at the edge of the coverage area (satellite at the horizon).
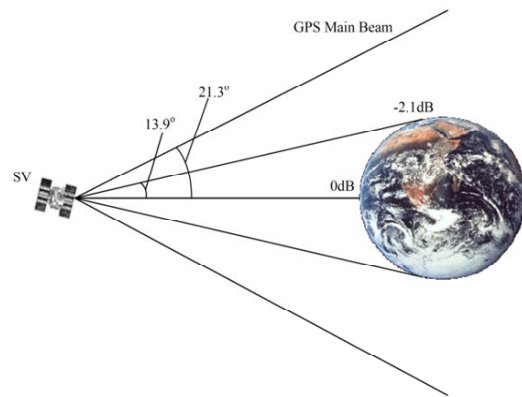
Fig. 10 GPS Satellite Antenna Coverage

The difference in signal strength caused by this variation in path length is about 2.1 dB. The GPS satellite antenna gain can be approximated by [7]:

$$G_T(dB) = 2.5413 * sinE - 2.5413 \qquad (14)$$

where E is the angle between the satellite zenith and the receiver (radians). The GPS receiver antenna shall accept the GPS navigation signals at both the L1 and L2 frequencies and output them to the GPS antenna electronics. The gain patterns of the TORNADO antennas, having -3dB gain at 10° elevation and 3.5dB at 90° elevation (Fig. 11) is approximated by:

$$G_R(dB) = 7.8659 * sinE - 4.3659 \qquad (15)$$
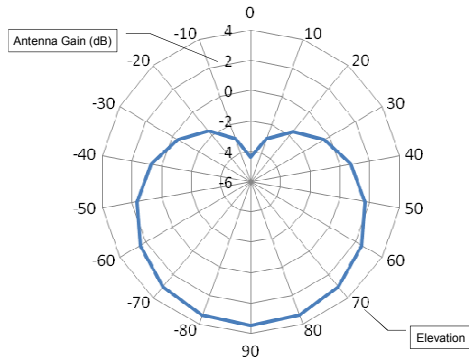
Fig. 11 TORNADO antenna gain pattern

GNSS signal frequencies (L-band) are sufficiently high to keep the ionospheric delay effects relatively small. On the other hand, they are not so high as to suffer severe propagation losses even in rainy conditions. However, the atmosphere causes small but nonnegligible effects that must be taken into account. The major effects that the atmosphere has on GNSS signals include [6]:

1) Ionospheric group delay/carrier phase advance;
2) Tropospheric group delay;
3) Ionospheric scintillation;
4) Tropospheric attenuation;
5) Tropospheric scintillation.

The first two effects have a significant impact on GNSS data accuracy but do not directly affect the received signal strength (C/N_0). Ionospheric scintillation is due to irregularities in the electron density of the Earth's ionosphere (scale size from hundreds of meters to kilometers), producing a variety of local diffraction and refraction effects. These effects cause short-term signal fading, which can severely stress the tracking capabilities of a GNSS receiver. Signal enhancements can also occur, but the GNSS user cannot make use of the brief periods of stronger signal in any useful manner. On the contrary, fading can be so severe that the signal level will drop below the receiver tracking threshold and, as a consequence, the signal must be re-acquired. Atmospheric scintillation effects are more significant in the equatorial and sub-equatorial regions and tend to be less of a factor at European and North-American latitudes. Unfortunately, at the moment, there is little to nothing we can do to estimate ionospheric scintillation effects and no efficient predictive algorithms are available for integration in the ABIA system. As a consequence the CIF functionality is not implemented for ionospheric fading and only a WIF approach is adopted (i.e., severe ionospheric scintillation causing loss of lock to the satellites). Tropospheric attenuation in the 1-2 GHz frequency band is dominated by oxygen, but even this effect is normally quite small [6]. The effects of water vapor, rain, and nitrogen attenuation in the GNSS frequency bands can be neglected for most applications [3]. The oxygen attenuation A(E) is on the order of 0.035dB for a satellite at zenith and varies with the elevation angle (E) in proportion to the tropospheric path length L (obliquity factor or mapping function). If the troposphere is modeled by a simple uniform

spherical shell of height h_m, the oxygen attenuation A(E) can be approximated by [6]:

$$A(E) \cong \frac{2A\left(\frac{\pi}{2}\right)\left(1+\frac{a}{2}\right)}{\sin E + \sqrt{\sin^2 E + 2a + a^2}} = \begin{cases} \frac{2A(90\,deg)}{\sin E + 0.043} dB & \text{for } 3 < E < 10\ deg \\ \frac{A(90\,deg)}{\sin E} dB & \text{for } E > 10\ deg \end{cases} \quad (16)$$

where:

a $=$ h_m/R_e
$h_m =$ Oxygen equivalent height ($h_m = 6km$)
$R_e =$ Earth radius ($R_e \cong 6378km$)

Equation (37) provides acceptable results only if E>3 degrees. However, since several other errors affects measurements from satellites with elevation below 5 degrees, a software mask is typically employed in avionics GNSS receivers to exclude these satellites form the navigation computations [1]. Tropospheric rainfall attenuation is of little importance in the GNSS frequency bands. For instance, at a frequency of 2 GHz the attenuation even for high rainfall rates (i.e., rates grater then 100 mm/h), is less than 0.01 dB/km. Rainfall attenuation below 2 GHz is even less. Tropospheric scintillation is caused by irregularities (primarily atmospheric turbulence) causing variations of the refractive index, mainly in the first few kilometres above the ground. Tropospheric scintillation effects vary with time and are dependent upon frequency and elevation angle. At GNSS frequencies, these effects are generally relatively small. The CCIR provided an expression for the long-term mean value of scintillation intensityσ_x. For small omnidirectional antennas, such as typical GNSS antennas, the CCIR expression for the long-term rms amplitude scintillation varies with frequency and elevation angle as follows [7]:

$$\sigma_m = 0.025 f^{\frac{7}{12}} (\csc E)^{-0.85} dB \quad (17)$$

where f is the frequency in GHz. For L1=1.57542GHz we have:

$$\sigma_m = 0.0326 (\csc E)^{-0.85} dB \quad (18)$$

Thus, for low elevation angles and small fractions of time, tropospheric scintillation can be significant, but otherwise it is quite small. The Noise Figure (in dB) is related to the system noise temperature (T_{Sys}) in Kelvin as follows [6]:

$$NF = 10 \log_{10}\left(1 + \frac{T_{Sys}}{T_0}\right) \quad (19)$$

where $T_0 = 290K = 24.6$ dB-K. The corresponding noise density, in W/Hz, is:

$$N_0 = K_B T_{Sys} \quad (20)$$

where $K_B =$ -228.6dBW/K-Hz (or 1.380×10^{-23} W/K-Hz), is the Boltzmann constant. The system noise temperature (antenna plus receiver) is computed using the Friisformula [8], [9]. Typical noise figures for state-of-the-art GPS receivers are between 2 and 4 dB. As an example of the overall SNR

computation, Fig. 12 shows the received SNR (signal transmitted from PRN-14) during the TORNADO turning descent maneuver.
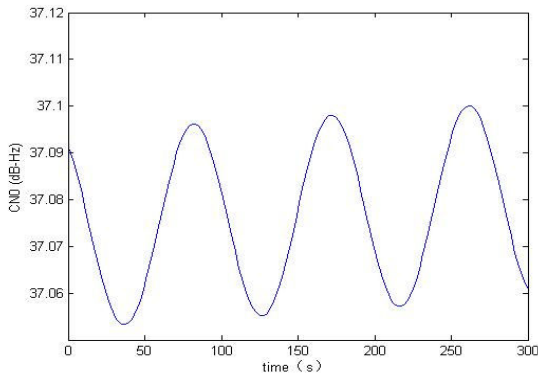

Fig. 12 PRN-14 SNR during turning descent

F. Multipath Analysis

Multipath is caused by the interference of multiple reflections (from the ground and the aircraft structure) with the direct signal transmitted by the satellite and represents a major source of error in the GNSS observations. The level and characteristics of the multipath effect depend on the geometry of the environment surrounding the antenna, the reflectivity of nearby objects/terrain and the satellite elevation angle. In order to builda reliable multipath model, a combination of SNR analysis (comparison with the direct GNSS signal) and geometric ray-tracing methods is adopted. In our case, we use the aircraft 3D CATIA model to identify the geometric characteristics of the multipath signal and study the SNR variations associated with multipath.
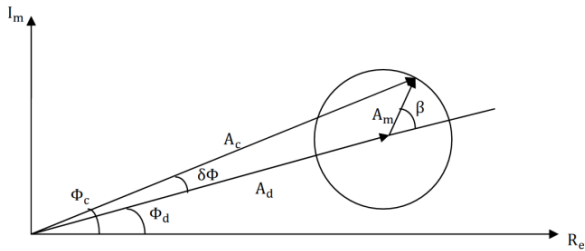
Fig. 13 Phase of GNSS signal

From Fig. 13, the SNR and phase error for a single refection can be represented as a function of direct and multipath signal amplitudes and the multipath relative phase β[10]:

$$SNR = A_c^2 = A_d^2 + A_m^2 + 2A_dA_m\cos\beta \qquad (21)$$

$$\tan(\delta_\phi) = \frac{A_m\sin\beta}{A_d + A_m\cos\beta} \qquad (22)$$

where A_d is the amplitude of the direct signal, A_m is the amplitude of the multipath signal andβ is the phase of the multipath.
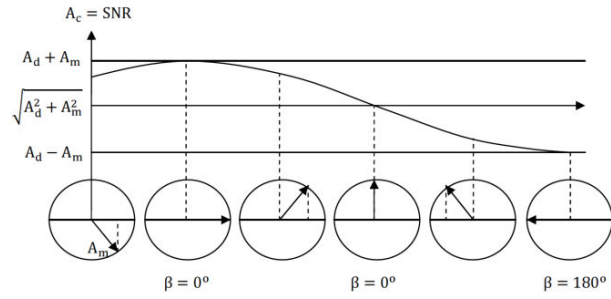
Fig. 14 Variation of Ac as function of the angle β

Fig. 14 shows that both the multipath phase $\beta$and the multipath signal amplitude affect the received signal. Therefore, we required a multipath model to simulate these two factors, considering the reflections from the aircraft surfaces (wings and fuselage) and from the ground. In our research, we adopted the Aeronautical Multipath Channel model developed during the ESA-SDS research [11]. Fig. 15 illustrates the structure of the multipath channel model. Let $h(t,\tau)$ be the impulse response of the multipath channel model. Then $h(t,\tau)$ is given by [10]:

$$h(t,\tau) = 1 + \sum_{i=1}^3 \sqrt{P_i} * n_i(t) * \delta(t - \tau_i) \qquad (23)$$

where P_i is the Echo Power of the ith path. The signal $n_i(t)$ is a noise signal with Power i, and a power spectral density $N(f)$[10]:

$$N(f) = \begin{cases} 0 & f < -B/2 \\ 1/B & -B/2 < f < B/2 \\ 0 & f > B/2 \end{cases} \qquad (24)$$

where B is the noise bandwidth. From the multipath channel model in Fig. 15, the wing reflection, the fuselage reflection and the ground echo are the main components of the multipath signal. Fig. 16 shows the geometric reflection model. The incoming wave is considered to be located T, a receiver at location R, and the reflection point at S. Location V is a defined point on the reflecting surface and n stands for a unit vector normal to the surface.

Fig. 15 Multipath channel model

Fig. 16 Geometric reflection model

In geometric ray-tracing theory, the reflection point S and the defined point V should satisfy the equation:

$$(S - V) \times n = 0 \tag{25}$$

And the line equation connecting T and R_{image}:

$$S = T + t \times (R_{image} - T) \tag{26}$$

where t is a parameter between 0 and 1. Combining (25) and (26):

$$S = T + \frac{n \times V - n \times T}{n \times (R_{image} - T)}(R_{image} - T) \tag{27}$$

The corresponding extra path length, L_{mS}, due to specular reflection, is then:

$$L_{mS} = |T - S| + |R - S| - |T - R| \tag{28}$$

In the TORNADO wing reflection model, the wing is assumed to be flat. By Gaussian Doppler Spectrum theory, the power of the wing echo spectrum is assumed to be [10], [12]:

$$P_{Gr(dB)} = 20 * \log_{10}\left(\frac{1}{\sqrt{2\pi\sigma^2}} * e^{-\frac{f^2}{2\sigma^2}}\right) \tag{29}$$

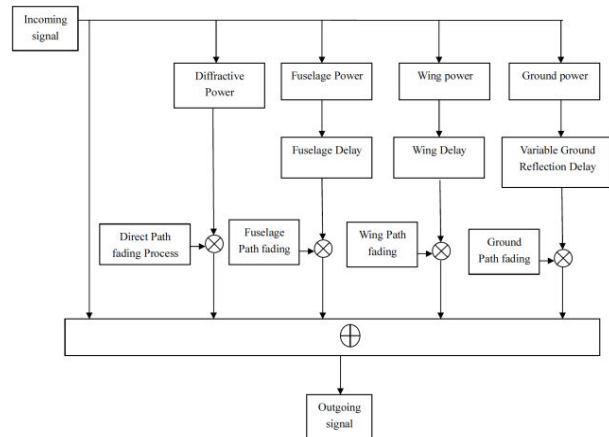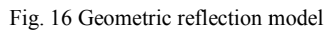where the deviation σ=3.8Hz. The wing reflection signal delay can be calculated from:

$$\tau_{wing}(t) = \frac{2 * L * \sin(E)}{C_0} \tag{30}$$

where L is the antenna height from the wing, E is the elevation angle and C_0 is the speed of light. In the ESA-SDS fuselage reflection model the fuselage is assumed to be a cylinder. The power of the fuselage echo spectrum is given by:

$$P_{proc}(dB) = 20 * \log_{10}(k + b_2 * e^{b_3 * |f|}) \tag{31}$$

where b_2 and b_3 are fuselage geometric coefficients described in [10], [11] and the constant k is given by:

$$k = -SNR - mean \, [dB] \tag{32}$$

ESA-SDS research [11] results showed that the fuselage reflection characteristics change very little by increasing the fuselage radius. For easier implementation of the fuselage reflection model, a 2-dimensional polynomial function of 4th order was fitted to each parameter (mean, b_2, b_3). In the case of TORNADO's upper antenna, since the antenna is located on the fuselage at a height of $L_{fuselage}$=0.05m, the fuselage reflection extra path is very short and the time delay $\tau_{fuselage} = 1.7 \times 10^{-10}$s. Ground reflection becomes important only during the landing phase, when the aircraft is in close proximity of the terrain. Like before, assuming a Gauss distributed ground reflection amplitude with zero mean, the ground echo power is given by [12]:

$$P_{Gr(dB)} = 20 * \log_{10}\left(\frac{1}{\sqrt{2\pi\sigma^2}} * e^{-\frac{f^2}{2\sigma^2}}\right) \tag{33}$$

where, in this case, the deviation σ=3.8Hz. Assuming that the airport/terrain is flat:

$$\tau_{ground}(t) = \frac{2 * h * \sin(E)}{C_0} \tag{34}$$

where h is the aircraft altitude and E is the elevation angle. Obviously, this basic ground echo model can be expanded to take into account various terrain geometries. As an example, Fig. 17 shows the ground echo signal time delay during a TORNADO turning descent maneuver over flat terrain. The simulation time is 300s.

Fig. 17 Ground echo time delay

As discussed in [6], GPS receivers can effectively reject most of the multipath signal if the differential delay $\Delta\tau > 1.5$ μs for the C/A code and 0.15μs for the P(Y) code. As a consequence, the region of potential multipath delay problems for the C/A code is:

$$h * \sin(E) < (1.5 \, \mu s) * C_0 = 448.5 \, m \tag{35}$$

Simulation results showed that the fuselage reflection is the main contribution to multipath. The effects of reflected signals from the wings and from the ground are comparatively small.

G. Doppler Shift Analysis

Doppler shift is the change in frequency of the received signal that is experienced when the observer (aircraft) moves relative to the signal source (satellite). The Doppler shift caused by satellite/aircraft relative motion is given by:

$$\Delta f_n = \left(\frac{v_i - v_u}{c}\right) \times f \times \cos\alpha_n \tag{36}$$

where:

Δf_n = n^{th} satellite signal frequency shift;
v_i = satellite velocity;
v_u = aircraft velocity;
c = speed of light(3×10^8 ms^{-1});
f = GPS frequency;
α_n = angle between the aircraft velocity and the nth satellite LOS vector.

Examples of the Doppler shift experienced by the signal received from a particular satellite (PRN-5) during straight-and-level flight and during turning-descent maneuvers are shown in Figs. 18 and 19.
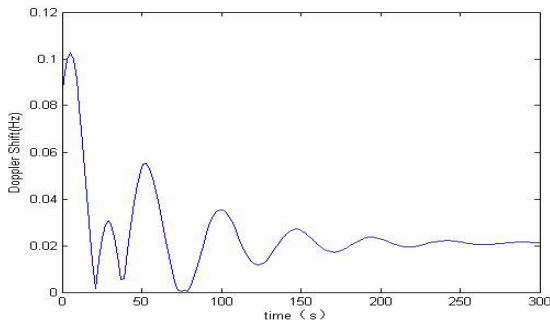

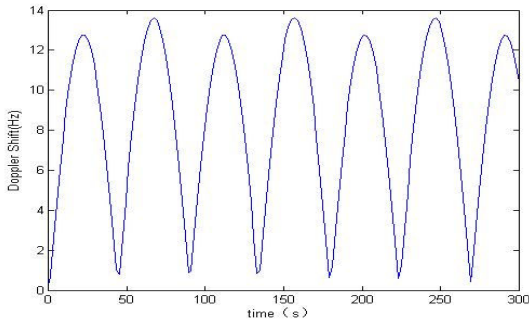Fig. 18 Doppler Shift (straight and level)

Fig. 19 Doppler Shift (turning descent)

H. Integrity Flag Criteria

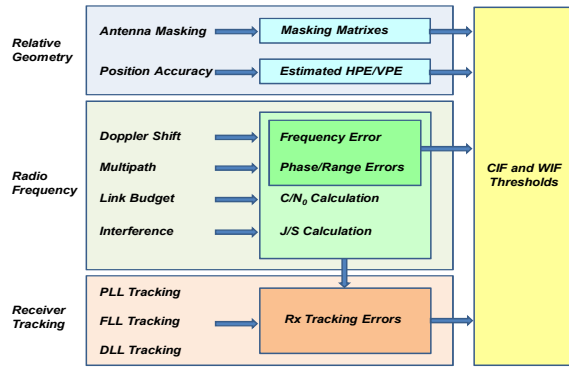The philosophy adopted to set-up thresholds for the ABIA CIF and WIF integrity flags is depicted in Fig. 20.

Fig. 20 Integrity flag thresholds

The masking integrity flag criteria are the following:
1) When the current aircraft maneuver will lead to less the 4 satellite in view, the CIF shall be generated.
2) When less than 4 satellites are in view, the WIF shall be generated.

Additionally, if only four satellites are in view:
3) When one (or more) satellite(s) elevation angle (antenna frame) is less than 10 degrees, the caution integrity flag shall be generated.
4) When one (or more) satellite(s) elevation angle is less than 5 degrees, the warning integrity flag shall be generated.

From the definition of Dilution of Precision (DOP) factors, GNSS accuracy can be expressed by [13]:

$$\sigma_P = DOP \times \sigma_{UERE} \tag{37}$$

where σ_P is the standard deviation of the positioning accuracy and σ_{UERE} is the standard deviation of the satellite pseudorange measurement error. For the C/A-code σ_{UERE} is in the order of 33.3m. Therefore, the 1-sigma Estimated Position, Horizontal and Vertical Errors of a GNSS receiver can be calculated using the PDOP (EPE in 3D), the HDOP (EHE in 2D) or the VDOP (EVE). In order to generate CIFs and WIFs that are consistent with current GNSS Required Navigation Performance (RNP), we need to introduce the Horizontal and Vertical Accuracy (HA/VA) requirements in the various flight phases. Table II shows the GNSS signal-in-space alert requirements in terms of HA/VA for En-route, Non-precision Approach (NPA) and for the three categories of Precision Approach. Table III shows the GNSS signal-in-space protection requirements [14], [15]. The Horizontal Alert Limit (HAL) is the radius of a circle in the horizontal plane, with its centre being at the true position, which describes the region which is required to contain the indicated horizontal position with the required probability for a particular navigation mode. Similarly, the Vertical Alert Limit (VAL) is half the length of a segment on the vertical axis, with its centre being at the true position, which describes the region which is required to contain the indicated vertical position with the required probability for a particular navigation mode.

TABLE II
SIGNAL-IN-SPACE ALERT REQUIREMENTS

Typical operation	Accuracy horizontal 95%	Accuracy vertical 95%
En-route	3.7 km	N/A
En-route Terminal	0.74km	N/A
NPA	220m	N/A
APV-I	16m	20m
APV-II	16m	8m
Category-I prec. approach	16m	6m-4m
Category-II prec. approach	6.9m	2m
Category-III prec. approach	6.2m	2m

Based on our discussion, the DOP integrity flags criteria are:

1) When the EHE exceeds the HA 95% or the VA 95% alert requirements, the CIF shall be generated.
2) When the EHE exceeds the HAL or the EVE exceeds the VAL, the WIF shall be generated.

TABLE III
SIGNAL-IN-SPACE PROTECTION REQUIREMENTS

Typical operation	Horizontal Alert Limit	Vertical Alert Limit	TTA
En-route	7.4 km	N/A	5min
En-route continental	3.7km	N/A	15s
En-route terminal	1.85 km	N/A	10s
NPA	556m	N/A	10s
APV-I	40m	50m	6s
APV-II	40m	20m	6s
Category-I prec. approach	40m	15m-10m	6s
Category-II prec. approach	17.3m	5.3m	1s
Category-III prec. approach	15.5m	5.3m	1s

During the landing phase, a GNSS Landing System (GLS) has to be augmented by GBAS in order to achieve the RNP, as well as Lateral and Vertical Protection Levels (LPL and VPL). LPL/VPL is defined as the statistical error value that bounds the Lateral/Vertical Navigation System Error (NSE) with a specified level of confidence. In particular, for the case of LAAS, which allows for multiple DGPS reference receivers (up to four) to be implemented, two different hypotheses are made regarding the presence of errors in the measurements:

1) H_0 Hypothesis – No faults are present in the range measurements (includes both the signal and the receiver measurements) used in the ground station to compute the differential corrections;
2) H_1 Hypothesis – A fault is present in one or more range measurements and is caused by one of the reference receivers used in the ground station.

Consequently, LPL and VPL are computed as follows:

$$LPL = MAX \{LPL_{H0}, LPL_{H1}\} \tag{38}$$

$$VPL = MAX \{VPL_{H0}, VPL_{H1}\} \tag{39}$$

VPL and LPL for the H_0 and H_1 hypotheses are calculated as described in [16]. The lateral and vertical accuracy (NSE 95%) and alert limits required by a GLS in the presence of LAAS, considering the continuously varying position of the aircraft with respect to the Landing Threshold Point (LTP) are given in [16]. Additionally, [16] provides the so-called Continuity of Protection Levels in terms of Predicted Lateral and Vertical Protection Levels (PLPL and PVPL). Although the definition in [16] is quite comprehensive, a generic statement is made that the PVPL and PLPL computations shall be based on the ranging sources expected to be available for the duration of the approach. In other terms, it is implied that the airborne subsystem shall determine which ranging sources are expected to be available, including the ground subsystem's declaration of satellite differential correction availability (satellite setting information). Unfortunately, this generic definition does not address the various conditions for satellite signal losses associated to specific aircraft maneuvers (including curved GLS precision approaches). Therefore, it is suggested that an extended definition of PLPL and PVPL is developed taking into account the continuously varying aircraft-satellite relative geometry (masking envelope). In particular, when the current aircraft manoeuvre will lead to less than 4 satellites in view or unacceptable accuracy degradations, the CIF shall be generated. Following our discussion, the additional integrity flags criteria adopted for GLS in the presence of LAAS are the following:

1) When the PLPL exceeds LAL or PVPL exceeds the VAL, the CIF shall be generated.
2) When the LPL exceeds the LAL or the VPL exceeds the VAL, the WIF shall be generated.

Multipath integrity flags were defined using the Early-Late Phase (ELP) observable and the range error. In a GPS receiver having three correlators (early, prompt and late), the phase of a correlator is given by [16]:

$$\Phi_C(t) = \tan^{-1}\left(\frac{Q_C}{I_C}\right) \tag{40}$$

where the subscript C can refer to early (E), prompt (P) and late (L) respectively. The prompt phase is always kept close to zero by the carrier tracking loop. Early and late correlators are then placed on each side of the prompt, which means one of the phase of the correlator is positive and the other is negative. So, the phase difference between the two is increased in the presence of multipath. ELP is simply the phase difference between the early and late correlator outputs, where the phase of a correlator output is equal to the inverse tangent of the Q channel output divided by the I channel output. Mathematically, ELP is calculated by [16]:

$$ELP(t) = \tan^{-1}\left[\frac{Q_L(t)}{I_L(t)} - \frac{Q_E(t)}{I_E(t)}\right] \tag{41}$$

The probability of multipath detection is approximately 80% by setting the ELP threshold 0.1 rad (Fig. 21).
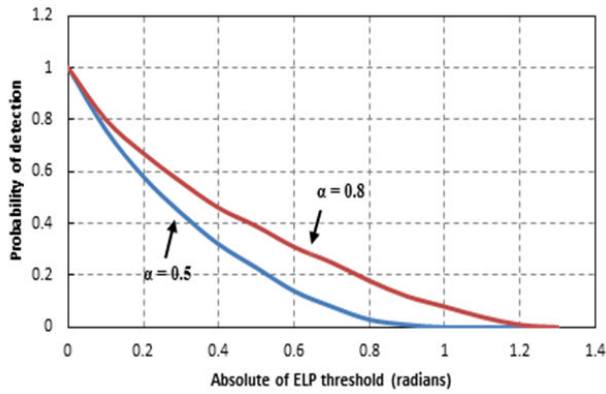
Fig. 21 Probability of detecting multipath for varying threshold on ELP value ($\alpha = A_m/A_d$) [17], [18]

Additionally, as shown in Fig. 21, with an ELP threshold of 0.1 radians, the probability of false alarm is 0.3 when C/N_0 is 42 dB/Hz.
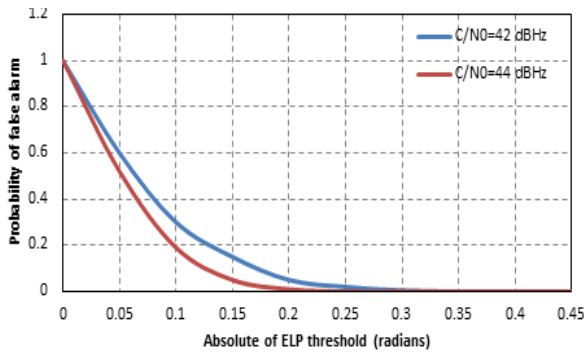

Fig. 22 Probability of false alarm for multipath detection for varying threshold on ELP value [17], [18]

As a result of our analysis, the multipath integrity flags criteria are the following:
1) When the ELP exceeds 0.1 radians, the caution integrity flag shall be generated.
2) When the multipath range error exceeds 1 meter, the warning integrity flag shall be generated.

The possibility of setting additional thresholds based on the multipath phase error is currently being investigated. In order to define the integrity thresholds associated with Doppler and Fading effects, a dedicated analysis of the GNSS receiver tracking performance was required. When the GNSS measurement errors exceed certain thresholds, the receiver loses lock to the satellites. Since both the code and carrier tracking loops are nonlinear, especially near the threshold regions, only Monte Carlo simulations of the GNSS receiver in different dynamics and SNR conditions can determine the receiver tracking performance [13], [18]. Nevertheless, some conservative rule of thumbs that approximate the measurement errors of the GNSS tracking loops can be used. Numerous sources of measurement errors affect the Phase Lock Loop (PLL) and the Frequency Lock Loop (FLL). However, for our purposes, it is sufficient to analyze the dominant error sources in each type of tracking loop. Considering a typical GNSS receivers employing a two-quadrant arctangent discriminator, the PLL threshold is given by [13]:

$$3\sigma_{PLL} = 3\sigma_j + \theta_e \leq 45° \qquad (42)$$

where:
σ_j = 1-sigma phase jitter from all sources except dynamic stress error
θ_e = dynamic stress error in the PLL tracking loop

Expanding (42), the 1-sigma threshold for the PLL tracking loop becomes [13]:

$$\sigma_{PLL} = \sqrt{\sigma_{tPLL}^2 + \sigma_\upsilon^2 + \theta_A^2} + \frac{\theta_e}{3} \leq 15° \qquad (43)$$

where:
σ_{tPLL} = 1-sigma thermal noise;
σ_υ = vibration-induced oscillator phase noise;
θ_A = Allan variance–induced oscillator jitter.

The PLL thermal noise is often thought to be the only carrier tracking error, since the other sources of PLL jitter may be either transient or negligible. The PLL thermal noise jitter is computed as follows:

$$\sigma_{tPLL} = \frac{360}{2\pi} \sqrt{\frac{B_n}{C/N_0}\left(1 + \frac{1}{2TC/N_0}\right)}\,(degrees) \qquad (44)$$

where:
B_n = carrier loop noise bandwidth (Hz);
C/N_0 = carrier to noise power ratio (dB-Hz);
T = predetection integration time (seconds);

B_n and C/N_0 can be derived from the SNR model described before. Determination of the vibration-induced oscillator phase noise is a complex analysis problem. In some cases, the expected vibration environment is so severe that the reference oscillator must be mounted using vibration isolators in order for the GPS receiver to successfully operate in PLL. The equation for vibration induced oscillator jitter is:

$$\sigma_\upsilon = \frac{360f_L}{2\pi} \sqrt{\int_{f_{min}}^{f_{max}} S_\upsilon^2(f_m) \frac{P(f_m)}{f_m^2} df_m}\,(degrees) \qquad (45)$$

where:
f_L = L-band frequency (Hz);
$S_\upsilon(f_m)$ = oscillator vibration sensitivity of $\Delta f/f_L$ per g as a function of f_m;
f_m = random vibration modulation frequency (Hz);
$P(f_m)$ = power curve of the random vibration as a function of $f_m (g^2/Hz)$;
g = gravity acceleration.

Usually the oscillator vibration sensitivity, $S_\upsilon(f_m)$ is not variable over the range of the random vibration modulation frequency, then (45) can be simplified to:

$$\sigma_\upsilon = \frac{360f_L S_\upsilon}{2\pi} \sqrt{\int_{f_{min}}^{f_{max}} \frac{P(f_m)}{f_m^2} df_m}\,(degrees) \qquad (46)$$

In the TORNADO simulation, we assume the random vibration power curve to be flat from 20Hz to 2000Hz with an amplitude of $0.005g^2/Hz$ and the oscillator vibration sensitivity $S_\upsilon(f_m) = 1 \times 10^{-9}$ parts/g. The equations used to determine Allan deviation phase noise are empirical. They are stated in terms of what the requirements are for the short-term stability of the reference oscillator as determined by the Allan variance method of stability measurement. The equation for second-order loop short-term Allan deviation is:

$$\theta_{A2} = 144 \frac{\sigma_A(\tau)*f_L}{B_n} \text{ (rad)} \qquad (47)$$

The equation for third–order loop short-term Allan deviation for PLL is [13]:

$$\theta_{A3} = 160 \frac{\sigma_A(\tau)*f_L}{B_n} \text{ (rad)} \qquad (48)$$

where:

$\sigma_A(\tau) = $ Allan deviation-induced jitter (degrees);
$f_L = $ L-band input frequency (Hz);
$\tau = $ short-term stability gate time for Allan variance measurement (seconds);
$B_n = $ noise bandwidth.

Usually $\sigma_A(\tau)$ can be determined for the oscillator and it changes very little with gate time τ. In our research, the loop filter is assumed as a third-order with a noise bandwidth B_n=18Hz and the gate time $\tau = 1/B_n = 56$ms. The Allan deviation is specified to be $\sigma_A(\tau) = 10^{-10}$. The dynamic stress error depends on the loop bandwidth and order. In a third-order loop, the dynamic stress error is given by the following equation:

$$\theta_{e3} = \frac{d^3R/dt^3}{\omega_0^3} = 0.4828 \frac{\frac{d^3R}{dt^3}}{B_n^3} \text{ (degrees)} \qquad (49)$$

where:

$d^2R/dt^2 = $ maximum LOS acceleration dynamics ($°/s^2$);
$B_n = $ noise bandwidth.

Considering the TORNADO GPS receiver characteristics, a third-order loop noise bandwidth is 18Hz and the maximum LOS jerk dynamic stress is $10g/s$=$98m/s^3$[14].For the L1 frequency we have: $d^3R/dt^3 = (98/s^3) \times (360°/cycle) \times (1575.42 \times 10^6 \text{ cycles/s})/c = 185398°/s^3$.

Frequency jitter due to thermal noise and dynamic stress error are the main errors in a GNSS receiver FLL. The receiver tracking threshold is such that the 3-sigma jitter must not exceed one-fourth of the frequency pull-in range of the FLL discriminator. Therefore, the FLL tracking threshold is [13]:

$$3\sigma_{FLL} = 3\sigma_{tFLL} + f_e \leq 1/4T \text{ (Hz)} \qquad (50)$$

where:

$3\sigma_{FLL} = $ 3-sigma thermal noise frequency jitter
$\sigma_{tFLL} = $ dynamic stress error in the FLL tracking loop

Equation (50) shows that the dynamic stress frequency error is a 3-sigma effect and is additive to the thermal noise frequency jitter. The reference oscillator vibration and Allan deviation–induced frequency jitter are small-order effects on the FLL and are considered negligible. The 1-sigma frequency jitter threshold is 1/(12T) = 0.0833/T Hz. The FLL tracking loop jitter due to thermal noise is:

$$\sigma_{tFLL} = \frac{1}{2\pi T} \sqrt{\frac{4FB_n}{C/N_0} \left[1 + \frac{1}{TC/N_0}\right]} \text{ (Hz)} \qquad (51)$$

where F is 1 at high C/N_0 and 2 near the threshold. σ_{tFLL} is independent of C/A or P(Y) code modulation and loop order. Since the FLL tracking loop involves one more integrator that the PLL tracking loop of the same order [14], the dynamic stress error is:

$$f_e = \frac{d}{dt}\left(\frac{1}{360\omega_0^n} \frac{d^nR}{dt^n}\right) = \frac{1}{360\omega_0^n} \frac{d^{n+1}R}{dt^{n+1}} \text{ (Hz)} \qquad (52)$$

Regarding the code tracking loop, a conservative rule-of-thumb for the Delay Lock Loop (DLL) tracking threshold is that the 3-sigma value of the jitter due to all sources of loop stress must not exceed the correlator spacing (d), expressed in chips. Therefore [4], [13]:

$$3\sigma_{DLL} = 3\sigma_{tDLL} + R_e \leq d \text{ (chips)} \qquad (53)$$

where:

$\sigma_{tDLL} = $ 1-sigma thermal noise code tracking jitter;
$R_e = $ dynamic stress error in the DLL.

The DLL thermal noise code tracking jitter is given by:

$$\sigma_{tDLL} = \sqrt{\frac{4F_1d^2B_n}{c/n_0} \left[2(1-d) + \frac{4F_2d}{Tc/n_0}\right]} \text{ (Hz)} \qquad (54)$$

where:

$F_1 = $ DLL discriminator correlator factor (1 for time shared tau-dithered early/late correlator and 0.5 for dedicated early and late correlators);
$d = $ Correlator spacing between early, prompt and late;
$B_n = $ Code loop noise bandwidth;
$F_2 = $ DLL dicriminator type factor (1 for early/late type discriminator and 0.5 for dot product type discriminator).

The DLL tracking loop dynamic stress error is given by:

$$R_e = \frac{\frac{dR^n}{dt^n}}{\omega_0^n} \text{ (chips)} \qquad (55)$$

where dR^n/dt^n is expressed in chips/sec^n.

The PLL, FLL and DLL error models (conservative rule-of-thumb equations) described above allow to determine the C/N_0 corresponding to the tracking threshold of the receiver. A generic criteria applicable to the ABIA system is:

$$\left(\frac{C}{N_0}\right)_{Threshold} = \max\left[\left(\frac{C}{N_0}\right)_{PLL}, \left(\frac{C}{N_0}\right)_{FLL}, \left(\frac{C}{N_0}\right)_{DLL}\right] \qquad (56)$$

where:

$(C/N_0)_{PLL}$ = Minimum C/N_0 for PLL tracking;

$(C/N_0)_{FLL}$ = Minimum C/N_0 for FLL tracking;

$(C/N_0)_{DLL}$ = Minimum C/N_0 for DLL tracking.

Numerical solutions of (42), (50) and (53) show that the weak link in unaided avionics GNSS receivers is the carrier tracking loop threshold (greater sensitivity to dynamics stress). Therefore, the $(C/N_0)_{PLL}$ threshold can be adopted in these cases. In general, when the PLL loop order is made higher, there is an improvement in dynamic stress performance. Therefore, third order PLL are widely adopted in avionics GNSS receivers. Assuming 15 to 18 Hz noise bandwidth and 5 to 20 msec predetection integration time (typical values for avionics receivers), the rule-of-thumb tracking threshold for the PLL gives 25 to 28 dB-Hz. Additionally, in aided avionics receiver applications, the PLL tracking threshold can be significantly reduced by using external velocity aiding in the carrier tracking loop. With this provision, a tracking threshold of approximately 15 to 18 dB-Hz can be achieved. Using these theoretical and experimental threshold values, we can also calculate the receiver Jamming-to-Signal (J/S) performance for the various cases of practical interest, as described in [19]. When available, Monte Carlo simulation and flight test data collected in representative portions of the aircraft operational flight envelope shall be used. Taking an additional 5% margin on the 3-sigma tracking thresholds for the CIF, the following additional criteria are introduced:

1) When either $42.25° \leq 3\sigma_{PLL} \leq 45°$ or $0.2375T \leq 3\sigma_{FLL} \leq 0.25T$ or $0.05d \leq 3\sigma_{DLL} \leq d$, the CIF shall be generated.

2) When either $3\sigma_{PLL} > 45°$ or $3\sigma_{FLL} > 1/4T$ or $3\sigma_{DLL} > d$ the WIF shall be generated.

In avionics receiver, lock detectors are used to assess if the satellite signals are being tracked or not tracked. Code lock detection is very similar to estimating the received C/N_0, inferring that the receiver is operating on or near the correlation peak. Knowledge of code lock is obviously parallel to the knowledge of received signal power. The receiver's code-correlation process has to raise the signal out of the noise. The spread spectrum processing gain (G_p) is defined as the ratio of the spread bandwidth to the unspread (baseband) bandwidth and is expressed in dB. The post-correlation signal-to-noise ratio can be calculated by [12]:

$$(S/N)_{post-corr.} = (S/N)_{pre-corr.} + G_p \qquad (57)$$

When the receiver code is aligned with the transmitted code, the signal power at the bandpass output is crushed into approximately 100 Hz of bandwidth. The processing gain can be calculated from:

$$G_P = 10 \log\left(\frac{2C_R}{T_D}\right) \text{ (dB)} \qquad (58)$$

where C_R is the chipping rate and T_D is the data period. For the C/A-code this works out to be about 43dB. The TORNADO-IDS receiver has a cut off value at 10dB, which means that if the value is less than this the satellite signal level is too low to be used in the positioning computations [12]. Therefore, an additional threshold to be accounted for is:

$$S/N_{post-corr.} = S/N_{pre-corr.} + G_p \geq 10 \text{ dB} \qquad (80)$$

During the GPS-TSPI flight test activities performed on TORNADO-IDS with unaided L1 C/A code avionics receivers, it was also found that, in all dynamics conditions explored, a C/N_0 of 25 dB-Hz was sufficient to keep tracking of the satellites [15]. Consequently, taking a 2 dB margin for the CIF, the following additional criteria are adopted for the TORNADO S/N integrity flags:

1) When the C/N_0 is less than 27dB-Hz or the difference between the S/N and the processing gain is less than 12 dB, the CIF shall be generated.

2) When the C/N_0 is less than 25dB-Hz or the difference between the S/N and the processing gain is less than 10 dB, the WIF shall be generated.

V. SIMULATION

In order to validate the design validate the ABIA IFG module, a MATALAB simulation was performed employing the algorithms developed during this research. The simulated TORNADO aircraft trajectory included the following phases:

1) Climb flight phase (0-5min);
2) Cruise flight phase (5-10min);
3) Turn and descend flight phase (10-5min);
4) Cruise flight phase (15-20min);
5) Straight descent flight phase (20-25min).

In this simulation, the cruise phases corresponded to straight-and-level flight segments. During the simulation, three cases of satellite constellation were considered:

1) GPS only;
2) GALILEO only;
3) Combined GPS/GALILEO.

All CIFs and WIFs relative to antenna masking, geometric accuracy degradations, SNR, multipath and Doppler shift were generated. The main results obtained with the simulated GPS constellation are shown in Table IV.

TABLE IV
TORNADO INTEGRITY FLAGS

Phase	Climb	Cruise	Turn & Descent	Cruise	Appr.
Duration	5min	5min	5min	5min	5min
Satellites in view	PRN 1, 3, 6, 7, 9, 11, 12, 13, 14, 15, 22, 23, 26, 27, 30, 31				
CIF	-	-	600~608s 672~698s 762~788s 852~878s	-	1484~1500s
WIF	-	-	674~692s 764~782s 854~872s	-	1490~1500s

Table V shows the specific CIFs and WIFs generated during the various TORNADO flight phases. There was only one case (flight slice 600-608s) where the CIF was generated not being followed by the WIF (this was due to a temporary adverse relative geometry during the turning descent maneuvers). In all other cases, the CIF was followed by the WIF. It was also observed that the CIF was always triggered at least 2 seconds before the successive WIF onset (up to 6 seconds during the straight descent phase). These results contribute to corroborate the validity of the models developed for the CIF/WIF thresholds. It was also observed that the CIF was always triggered at least 2 seconds before the successive

WIF onset. This evidence is particularly important for the ABIA system design. In fact, it is evident that the availability of a usable CIF represents a significant progress in this research with the potential for both manned aircraft and UAS's to recover from mission- and safety-critical flight conditions potentially leading to GNSS data losses. Therefore, it is envisaged that a properly designed ABIA FPM could take full advantage of this predictive behavior, allowing the aircraft to correct its flight trajectory/attitude in order to avoid the occurrence of the critical GNSS data losses. Additionally, it is possible that this predictive behavior be exploited in the pursuit of a GNSS based auto-landing capability.

TABLE V
CIF AND WIF IN VARIOUS FLIGHT PHASES

Phase	Climb	Cruise	Turn & Descent	Cruise	Approach
Duration	5min	5min	5min	5min	5min
Masking CIF	0~300s PRN 30	300~600s PRN 30	PRN 3, 6, 11, 12, 13, 14, 15, 22, 23, 26	900~1200s PRN 30	1200~1500s PRN 30
Masking WIF	-	-	PRN 3, 6, 11, 12, 13, 14, 15, 22, 23, 26	-	PRN 30 1210~1236s 1254~1500s
SNR CIF	0~300s PRN 1, 3, 9, 11, 12, 13, 30	300~600s PRN 1, 3, 9, 11, 12, 13, 30	600~900s PRN. 1, 3, 12, 13, 30	900~1200s PRN.1, 3, 9, 11, 12, 13, 30	1200~1500s PRN. 1, 3, 9, 11, 12, 13, 30
SNR WIF	0~300s PRN. 1, 3, 11, 12, 13, 30 0~50s PRN.9	300~600s PRN. 1, 3, 11, 12, 13, 30	600~900s PRN. 1, 3, 12, 13, 30	900~1200s PRN.1, 3, 11, 12, 13, 30	1200~1500s PRN 1, 3, 11, 12, 13, 30
Multipath CIF	0~300s PRN 1, 3, 7, 9, 11, 12, 13, 30	300~600s PRN 1, 3, 7, 9, 11, 12, 13, 30	600~900s PRN 1, 3, 7, 9, 11, 12, 13, 30	900~1200s PRN 1, 3, 7, 9, 11, 12, 13, 30	1200~1500s PRN 1, 3, 11, 12, 13, 30
Multipath WIF	0~300s PRN 1, 3, 7, 9, 11, 12, 13, 30	300~600s PRN 1, 3, 7, 9, 11, 12, 13, 30	600~900s PRN 1, 3, 7, 9, 11, 12, 13, 30	900~1200s PRN 1, 3, 7, 9, 11, 12, 13, 30	1200~1500s PRN 1, 3, 11, 12, 13, 30
Doppler CIF	0~300s PRN 1, 3, 7, 9, 11, 12, 13, 30	300~600s PRN 1, 3, 7, 9, 11, 12, 13, 30	600~900s PRN 1, 3, 7, 9, 11, 12, 13, 30	900~1200s PRN 1, 3, 7, 9, 11, 12, 13, 30	1200~1500s PRN 1, 3, 11, 12, 13, 30
Doppler WIF	0~300s PRN 1, 3, 7, 9, 11, 12, 13, 30	300~600s PRN 1, 3, 7, 9, 11, 12, 13, 30	600~900s PRN 1, 3, 7, 9, 11, 12, 13, 30	900~1200s PRN 1, 3, 7, 9, 11, 12, 13, 30	1200~1500s PRN 1, 3, 11, 12, 13, 30

VI. CONCLUSIONS AND FUTURE WORK

The architecture of a novel ABIA system for mission- and safety-critical GNSS applications was presented. The detailed design of the ABIA IFG module was also accomplished. This module can generate both CIFs and WIFs associated to antenna obscuration, geometric accuracy degradations, SNR, multipath and Doppler shift. A simulation of the IFG module was performed in MATLAB. Relevant flight maneuvers were considered in this simulation, including climb, cruise, turning descent and straight descent. From the results of this simulation activity, the following conclusions are drawn:

1) The initial design of an Avionics Based Integrity Augmentation (ABIA) system for GNSS applications was accomplished.
2) The ABIA Integrity Flag Generator (IFG) is capable of generating integrity flag to provide both caution (predictive) and warning signals to the pilot when GNSS

signals are degraded or lost.
3) According to the simulation results, after the CIF is generated, the time available for the pilot/autopilot to react (before the WIF is generated), is sufficient for safety-critical tasks including GLS curved/segmented precision approach and automatic landing applications.
4) Preliminary data analysis shows that the ABIA system can provide the TTA required for CAT-IIIC precision approach, which is currently unavailable with GBAS.

Further research is currently focusing on the following key areas [20]-[23]:

1) Improve the aircraft dynamics model and develop a Maneuver Identification Algorithm (MIA) suitable for incorporation in the ABIA Flight Path Guidance (FPG) module.
2) Examine other types of manned aircraft (e.g., civil airliners) and UAS, as well as unconventional body

shapes (e.g., blended wing body aircraft).

3) Perform additional research on multipath detection and isolation in various kinds of receiver for avionics applications.

4) Develop and test the ABIA Flight Path Guidance (FPG) modules for manned A/C and UAS.

The long-term objectives of this research comprise an in-depth evaluation of the ABAS/ABIA techniques potential to improve integrity levels in a wide spectrum of civil/military mission-critical and safety-critical GNSS applications. In particular, future research will address the following topics:

1) Investigating and comparing different types of avionics sensor technologies and their potential to support the design of a robust ABAS/ABIA architecture in small UA applications [24]-[29].

2) Evaluating the potential of ABAS/ABIA techniques to supplement current and likely future SBAS/GBAS technology for en-route, terminal, approach and surface aircraft/UAS operations.

3) Investigating the potential of ABAS/ABIA to support a UAS Sense-and-Avoid (SAA) capability [30].

4) Investigating the potential of ABAS/ABIA to enhance the performance of Flight Management Systems (FMS) for manned and unmanned aerospace vehicles [31]-[33].

5) Investigating the potential of ABAS/ABIA architectures to support ATM Intent Based Operations (IBO) in a four-dimensional trajectory (4DT) optimization environment [34]-[38].

REFERENCES

[1] Sabatini, R., and G. B. Palmerini, "Differential Global Positioning System (DGPS) for Flight Testing", NATO Research and Technology Organization (RTO), Systems Concepts and Integration Panel (SCI), AGARDograph Series RTO-AG-160, Vol. 21, Oct 2008.

[2] Ochieng W.Y., Sauer, K., Walsh, D., Brodin, G., Griffin, S., and Denney, M., "GPS Integrity and Potential Impact on Aviation Safety". The Journal of Navigation (Royal Institute of Navigation), Vol. 56, pp. 51–65. 2003.

[3] CelesTrak (CSSI) YUMA GPS Almanacs. Available online at: http://www.celestrak.com/GPS/almanac/Yuma/definition.asp (accessed in July 2012).

[4] CelesTrak (CSSI) SEM GPS Almanacs. Available online at:http://www.celestrak.com/GPS/almanac/SEM/definition.asp (accessed in July 2012).

[5] Anonymous, "Aircraft Drawings," available online at: http://www.aircraftdrawindsdownload.com (accessed in July 2012).

[6] Spilker, J. J., Global Positioning System: Theory and Applications, Vol. 1, American Institute of aeronautics and Astronautics publication, Inc., Reston, 1996.

[7] Gustavsson, P., "Development of a Matlab-based GPS-constellation simulation for navigation algorithm developments," MSc Thesis, Lulea University of Technology, 2005.

[8] Davenport, W. B., and Root, W.L., An Introduction to the Theory of Random Signals and Noise, IEEE Press, New York, 1987.

[9] Friis, H. T., "Noise Figures in Radio Receivers," Proceedings of the IRE, Vol. 32, July 1944, pp. 419-422.

[10] Steingass, A., "The High Resolution Aeronautical Multipath Navigation Channel," German Aerospace Center DLR, 2004. Available at http://www.kn-s.dlr.de/satnav.

[11] A. Steinggass, A. Lehner, "Aeronautical Channel Model". German Aerospace Center DLR. 2004. Available online at http://www.kn-s.dlr.de/satnav (accessed in July 2012).

[12] Braasch, M. S., "On the characterization of multipath errors in satellite-based precision approach and landing systems," MSc Thesis, College of Engineering and Technology, Ohio University, June 1992.

[13] Kaplan, E. D., Hegarty, C. J., Understanding GPS: Principles and Applications, Second Edition, Artech House, Boston and London, 2006.

[14] ICAO - Annex 10 to the Convention on International Civil Aviation, Aeronautical Telecommunications Volume 1: Radio Navigation Aids, Edition 6, July 2006.

[15] CAA Safety Regulation Group Paper 2003/09, GPS Integrity and Potential Impact on Aviation Safety. 2003.

[16] RTCA DO-245A, Minimum Aviation System Performance Standards for Local Area Augmentation System (LAAS), Dec 2004.

[17] Mubarak O. M., Dempster, A. G., "Analysis of early late phase in single and dual frequency GPS receivers for multipath detection," University of New South Wales (Australia). 2010. Available online at: http://www.gmat.unsw.edu.au/snap/staff/omer_mubarak.htm (accessed in July 2012).

[18] Mubarak, O. M., Dempster, A. G., "Statistical analysis of early late phase for multipath detection," IGNSS Symposium 2009, Gold Coast, Australia, December 2009.

[19] Ward, P, "Using a GPS Receiver Monte Carlo Simulator to Predict RF Interference Performance," Proceedings of the 10th International Technical Meeting of The Satellite Division of The Institute of Navigation, Kansas City, MO, September 1997, pp.1473–1482.

[20] R. Sabatini, T. Moore, C. Hill. "A New Avionics Based GNSS Integrity Augmentation System: Part 2 – Integrity Flags." Journal of Navigation (Royal Institute of Navigation), Vol. 66, No. 4, pp. 511-522. DOI: 10.1017/S0373463313000143. June 2013.

[21] R. Sabatini, T. Moore and C. Hill. "A New Avionics Based GNSS Integrity Augmentation System: Part 1 – Fundamentals." Journal of Navigation (Royal Institute of Navigation). Vol. 66, No. 3, pp. 363-383. DOI: 10.1017/S0373463313000027. May 2013.

[22] R. Sabatini, T. Moore and C. Hill. "Avionics Based GNSS Integrity Augmentation for Mission- and Safety-Critical Applications." 25th International Technical Meeting of the Satellite Division of the Institute of Navigation: ION GNSS-2012. Nashville (Tennessee), September 2012.

[23] R. Sabatini, T. Moore and C. Hill. "A Novel Avionics Based GNSS Integrity Augmentation System for Manned and Unmanned Aerial Vehicles." Paper presented at the European Navigation Conference 2012 (ENC 2012). Gdansk (Poland), April 2012.

[24] R. Sabatini, S. Ramasamy, A. Gardi and L. Rodriguez Salazar, "Low-cost Sensors Data Fusion for Small Size Unmanned Aerial Vehicles Navigation and Guidance."International Journal of Unmanned Systems Engineering, Vol. 1, No. 3, pp. 16-47. DOI: 10.14323/ijuseng.2013.11. August 2013.

[25] R. Sabatini, M.A. Richardson, C. Bartel, A. Kaharkar, T. Shaid, L. Rodriguez and A. Gardi, "A Low-cost Vision Based Navigation System for Small Size Unmanned Aerial Vehicle Applications." Journal of Aeronautics and Aerospace Engineering, Vol. 2, No. 3.DOI: 10.4172/2168-9792.1000110. May 2013.

[26] R. Sabatini, L. Rodríguez, A. Kaharkar, C. Bartel and T. Shaid, "Carrier-phase GNSS Attitude Determination and Control for Small UAV Applications." Journal of Aeronautics and Aerospace Engineering, Vol. 2, No. 4.DOI: 10.4172/2168-9792.1000120. July 2013.

[27] R. Sabatini, C. Bartel, A. Kaharkar, T. Shaid, D. Zammit-Mangion and H. Jia. "Vision Based Sensors and Multisensor Systems for Unmanned Aerial Vehicles Navigation and Guidance." Paper presented at the European Navigation Conference 2012 (ENC 2012). Gdansk (Poland), April 2012.

[28] R. Sabatini, L. Rodríguez, A. Kaharkar, C. Bartel and T. Shaid. "Satellite Navigation Data Processing for Attitude Determination and Control of Unmanned Air Vehicles." European Navigation Conference 2012, Paper presented at the European Navigation Conference 2012 (ENC 2012). Gdansk (Poland), April 2012.

[29] R. Sabatini, C. Bartel, A. Kaharkar, T. Shaid, H. Jia, and D. Zammit-Mangion."Design and Integration of Vision-based Navigation Sensors for Unmanned Aerial Vehicles Navigation and Guidance."SPIE Photonics Europe 2012 Conference. Brussels (Belgium), March 2012.

[30] L. Rodriguez Salazar, R. Sabatini, S. Ramasamy and A. Gardi."A Novel System for Non-Cooperative UAV Sense-And-Avoid."European Navigation Conference 2013 (ENC 2013). Vienna (Austria), April 2013.

[31] S. Ramasamy, R. Sabatini, A. Gardi, Y. Liu, "Novel Flight Management System for Real-Time 4-Dimensional Trajectory Based Operations." AIAA GNC 2013 Conference. London (USA). Boston, Massachusetts (USA), August 2013.

[32] M. Sangam, R. Sabatini, S. Ramasamy and A. Gardi, "Advanced Flight Management System for an Unmanned Reusable Space Vehicle."

International Journal of Unmanned Systems Engineering, Vol. 1, No. 3, pp. 48-68. DOI: 10.14323/ijuseng.2013.12. August 2013.

[33] S. Ramasamy, R. Sabatini, Y. Liu, A. Gardi, L. Rodriguez Salazar. "A Novel Flight Management System for SESAR Intent Based Operations."European Navigation Conference 2013 (ENC 2013). Vienna (Austria), April 2013.

[34] A. Gardi, R. Sabatini, S. Ramasamy, K. de Ridder, "4-Dimensional Trajectory Negotiation and Validation System for the Next Generation Air Traffic Management."AIAA GNC 2013 Conference. Boston, Massachusetts (USA), August 2013.

[35] A. Gardi, R. Sabatini, K. De Ridder, S. Ramasamy. L. Rodriguez Salazar. "Automated Intent Negotiation and Validation System for 4-Dimensional Trajectory Based Operations." European Navigation Conference 2013 (ENC 2013). Vienna (Austria), April 2013.

[36] K. Chircop, D. Zammit-Mangion, R. Sabatini."Bi-Objective Pseudospectral Optimal Control Techniques for Aircraft Trajectory Optimisation." 28th International Congress of the Aeronautical Sciences: ICAS-2012. Brisbane (Australia), September 2012.

[37] W. Camilleri, K. Chircop, D. Zammit-Mangion, R. Sabatini, V. Sethi, "Design and Validation of a Detailed Aircraft Performance Model for Trajectory Optimization." Paper presented at the AIAA MST Conference 2012. Minneapolis, Minnesota (USA), August 2012.

[38] W. Gu, R. Navaratne, D. Quaglia, Y. Yu., K. Chircop, I. Madani, H. Jia, V. Sethi, R. Sabatini, D. Zammit-Mangion, "Towards the Development of a Multi-disciplinary Flight Trajectory Optimization Tool — GATAC." ASME Turbo Expo 2012 Conference. Copenhagen (Denmark), June 2012.